ASM Handbook, Volume 15: Casting
ASM Handbook Committee, p 449-461
DOI: 10.1361/asmhba0005238

Modeling of Stress, Distortion, and Hot Tearing

Brian G. Thomas, University of Illinois (UIUC)
Michel Bellet, Centre de Mise en Forme des Matériaux (CEMEF)

COMPUTATIONAL MODELING of mechanical behavior during solidification is becoming more important. Thermal and microstructural simulations alone are insufficient to predict the quality of the final product that is desired by the casting industry. Accurate calculation of displacements, strains, and stresses during the casting process is needed to predict residual stress and distortion and defects such as the formation of cracks such as hot tears. It also helps predict porosity and segregation. As computing power and software tools for computational mechanics advance, it is becoming increasingly possible to perform useful mechanical analysis of castings and these important related behaviors.

The thermomechanical analysis of castings presents a formidable challenge for many reasons:

- Many interacting physical phenomena are involved in stress-strain formation. Stress arises primarily from the mismatch of strains caused by large temperature gradients and depends on the time- and microstructure-dependent inelastic flow of the material.
- Predicting distortions and residual stresses in cast products requires calculation of the history of the cast product and its environment over huge temperature intervals. This makes the mechanical problem highly nonlinear, involving liquid/solid interaction and complex constitutive equations. Even identifying the numerous metallurgical parameters involved in those relations is a daunting task.
- The coupling between the thermal and the mechanical problems is an additional difficulty. This coupling comes from the mechanical interaction between the casting and the mold components, through gap formation or the buildup of contact pressure, locally modifying the heat exchange. This adds some complexity to the nonlinear heat transfer resolution.
- Accounting for the mold and its interaction with the casting makes the problem multidomain, usually involving numerous deformable components with coupled interactions.
- Cast parts usually have very complex three-dimensional shapes, which puts great demands on the interface between CAD design and the mechanical solvers and on computational resources.
- The important length scales range from micrometers (dendrite arm shapes) to tens of meters (metallurgical length of a continuous caster), with similarly huge order-of-magnitude range in time scales.

This article summarizes some of the issues and approaches in performing computational analyses of mechanical behavior, distortion, and hot tearing during solidification. The governing equations are presented first, followed by a brief description of the methods used to solve them, and a few examples of recent applications in shape castings and continuous casting.

Governing Equations

The modeling of mechanical behavior requires solution of 1) the equilibrium or momentum equations relating force and stress, 2) the constitutive equations relating stress and strain, and 3) compatibility equations relating strain and displacement. This is because the boundary conditions specify either force or displacement at different boundary regions of the domain Ω:

$$\begin{aligned} \mathbf{u} &= \widehat{\mathbf{u}} \quad \text{on} \quad \partial\Omega_{\mathbf{u}} \\ \boldsymbol{\sigma}\,\mathbf{n} &= \widehat{\mathbf{T}} \quad \text{on} \quad \partial\Omega_{\mathbf{T}} \end{aligned} \qquad \text{(Eq 1)}$$

where $\widehat{\mathbf{u}}$ are prescribed displacements on boundary surface portion $\partial\Omega_{\mathbf{u}}$, and $\widehat{\mathbf{T}}$ are boundary surface forces or "tractions" on portion $\partial\Omega_{\mathbf{T}}$. The next sections first present the equilibrium and compatibility equations and then introduce constitutive equations for the different material states during solidification.

Equilibrium and Compatibility Equations. At any time and location in the solidifying material, the conservation of force (steady-state equilibrium) or momentum (transient conditions) can be expressed by:

$$\nabla \cdot \boldsymbol{\sigma} + \rho\mathbf{g} - \rho\frac{d\mathbf{v}}{dt} = 0 \qquad \text{(Eq 2)}$$

where $\boldsymbol{\sigma}$ is the stress tensor, ρ is the density, $\mathbf{g}$ denotes gravity, $\mathbf{v}$ is the velocity field, and d/dt denotes the total (particular) time derivation. Stress can be further split into the deviatoric stress tensor and the pressure field. The different approaches for simplifying and solving these equations are discussed in the section "Implementation Issues."

Once the material has solidified, the internal and gravity forces dominate, so the inertia terms in Eq 2 can be neglected. Furthermore, the strains that dominate thermomechanical behavior during solidification are on the order of only a few percent, otherwise cracks will form. With small gradients of spatial displacement, $\nabla\mathbf{u} = \partial\mathbf{u}/\partial\mathbf{x}$, and the compatibility equations simplify to (Ref 1):

$$\boldsymbol{\varepsilon} = \frac{1}{2}\left(\nabla\mathbf{u} + (\nabla\mathbf{u})^{\mathrm{T}}\right) \qquad \text{(Eq 3)}$$

where $\boldsymbol{\varepsilon}$ is the strain tensor and $\mathbf{u}$ is the displacement vector. This small-strain assumption simplifies the analysis considerably. The compatibility equations can also be expressed as a rate formulation, where strains become strain rates, and displacements become velocities. This formulation is more convenient for a transient computation with time integration involving fluid flow and/or large deformation.

In casting analysis, the cast material may be in the liquid, mushy, or solid state. Each of these states has different constitutive behavior, as discussed in the next three sections.

Liquid-State Constitutive Models. Metallic alloys generally behave as Newtonian fluids. Including thermal dilatation effects, the constitutive equation can be expressed as:

$$\dot{\boldsymbol{\varepsilon}} = \frac{1}{2\mu_{\mathrm{l}}}\mathbf{s} - \frac{1}{3\rho}\frac{d\rho}{dt}\mathbf{I} \qquad \text{(Eq 4)}$$

The strain-rate tensor $\dot{\boldsymbol{\varepsilon}}$ is split into two components: a mechanical part, which varies linearly with the deviatoric stress tensor $\mathbf{s}$, and a thermal part. In this equation, μ_{l} is the dynamic viscosity of the liquid, ρ is the density, and $\mathbf{I}$ is the

identity tensor. Taking the trace of this expression, $tr\dot{\boldsymbol{\varepsilon}} = \nabla \cdot \mathbf{v}$, the mass conservation equation is recovered:

$$\frac{d\rho}{dt} + \rho\nabla \cdot \mathbf{v} = \frac{\partial \rho}{\partial t} + \nabla \cdot (\rho \mathbf{v}) = 0 \qquad \text{(Eq 5)}$$

In casting processes, the liquid flow may be turbulent, even after mold filling. This may occur because of buoyancy forces or forced convection such as in jets coming out of the nozzle outlets in continuous casting processes. The most accurate approach, direct numerical simulation, generally is not feasible for industrial processes, owing to their complex-shaped domains and high turbulence. To compute just the large-scale flow features, turbulence models are used that increase the liquid viscosity according to different models of the small-scale phenomena. These models include the simple "mixing-length" models, the two-equation models such as *k*-ε, and large eddy simulation (LES) models, which have been compared with each other and with measurements of continuous casting (Ref 2–4).

Mushy-State Constitutive Models. Metallic alloys in the mushy state are two-phase liquid-solid media. Their mechanical response depends greatly on the local microstructural evolution, which involves several complex physical phenomena. An accurate description of these phenomena is useful for studying hot tearing or macrosegregation. Knowledge of the liquid flow in the mushy zone is necessary to calculate the transport of chemical species (alloying elements) (Ref 5). Knowledge of the deformation of the solid phase is important when it affects liquid flow in the mushy zone by "sponge-effects" (Ref 6). In such cases, two-phase models must be used. Starting from microscopic models describing the intrinsic behavior of the liquid phase and the solid phase, spatial averaging procedures must be developed to express the behavior of the compressible solid continuum and of the liquid phase that flows through it (Ref 7–9).

If a detailed description is not really needed, such as in the analysis of residual stresses and distortions, the mushy state can be approximated as a single continuum that behaves as a non-Newtonian (i.e., viscoplastic) fluid, according to Eq 6 to 8. Thus, the liquid phase is not distinguished from the solid phase, and the individual dendrites and grain boundaries are not resolved.

$$\dot{\boldsymbol{\varepsilon}} = \dot{\boldsymbol{\varepsilon}}^{\text{vp}} + \dot{\boldsymbol{\varepsilon}}^{\text{th}} \qquad \text{(Eq 6)}$$

$$\dot{\boldsymbol{\varepsilon}}^{\text{vp}} = \frac{3}{2K}(\dot{\varepsilon}_{\text{eq}})^{1-m}\mathbf{s} \qquad \text{(Eq 7)}$$

$$\dot{\boldsymbol{\varepsilon}}^{\text{th}} = -\frac{1}{3\rho}\frac{d\rho}{dt}\mathbf{I} \qquad \text{(Eq 8)}$$

K is the viscoplastic consistency and m the strain-rate sensitivity. Denoting $\sigma_{\text{eq}} = \sqrt{\tfrac{3}{2}s_{ij}s_{ij}}$ the von Mises equivalent stress scalar, and $\dot{\varepsilon}_{\text{eq}} = \sqrt{\tfrac{2}{3}\dot{\varepsilon}^{\text{vp}}_{ij}\dot{\varepsilon}^{\text{vp}}_{ij}}$ the von Mises equivalent strain-rate scalar, Eq 7 yields the well-known power law: $\sigma_{\text{eq}} = K(\dot{\varepsilon}_{\text{eq}})^m$. Note that the preceding Newtonian liquid model is actually a particular case of this non-Newtonian one: Eq 4 can be derived from Eq 6, 7, and 8 taking $m = 1$ and $K = 3\mu_{\text{l}}$. The solidification shrinkage is included in Eq 8: writing $\rho = g_{\text{s}}\,\rho_{\text{S}} + g_{\text{l}}\,\rho_{\text{L}}$ in the solidification interval (ρ_{S}, ρ_{L} densities at the solidus and liquidus temperatures, respectively, g_{s}, g_{l} volume fractions of solid and liquid, respectively), the thermal strain rate is defined as:

$$\text{tr}\dot{\varepsilon}^{\text{th}} = -\frac{1}{\rho}\frac{d\rho}{dt} = -\frac{1}{\rho}(\rho_{\text{S}} - \rho_{\text{L}})\frac{dg_{\text{s}}}{dt} \approx \frac{\rho_L - \rho_{\text{S}}}{\rho_L}\frac{dg_{\text{s}}}{dt} \qquad \text{(Eq 9)}$$

Solid-State Constitutive Models. In the solid state, metallic alloys can be modeled either as elastic-plastic or elastic-viscoplastic materials. In the latter class of models, one of the simpler models is expressed as follows, but it should be mentioned that a lot of models of different complexity can be found in the literature (Ref 10, 11).

$$\dot{\boldsymbol{\varepsilon}} = \dot{\boldsymbol{\varepsilon}}^{\text{el}} + \dot{\boldsymbol{\varepsilon}}^{\text{in}} + \dot{\boldsymbol{\varepsilon}}^{\text{th}} \qquad \text{(Eq 10)}$$

$$\dot{\boldsymbol{\varepsilon}}^{\text{el}} = \frac{1+\nu}{E}\dot{\boldsymbol{\sigma}} - \frac{\nu}{E}\text{tr}(\dot{\boldsymbol{\sigma}})\mathbf{I} + \dot{T}\frac{\partial}{\partial T}\left(\frac{1+\nu}{E}\right)\boldsymbol{\sigma} - \dot{T}\frac{\partial}{\partial T}\left(\frac{\nu}{E}\right)\text{tr}(\boldsymbol{\sigma})\mathbf{I} \qquad \text{(Eq 11)}$$

$$\dot{\boldsymbol{\varepsilon}}^{\text{in}} = \frac{3}{2\sigma_{\text{eq}}}\left\langle\frac{\sigma_{\text{eq}} - \sigma_0}{K}\right\rangle^{1/m}\mathbf{s} \qquad \text{(Eq 12)}$$

$$\dot{\boldsymbol{\varepsilon}}^{\text{th}} = -\frac{1}{3\rho}\frac{d\rho}{dt}\mathbf{I} \qquad \text{(Eq 13)}$$

The strain-rate tensor $\dot{\boldsymbol{\varepsilon}}$ is split into an elastic component, an inelastic (nonreversible) component, and a thermal component. Equation 11 is the hypoelastic Hooke's law, where E is Young's modulus, ν the Poisson's coefficient, and $\dot{\boldsymbol{\sigma}}$ a time derivative of the stress tensor $\boldsymbol{\sigma}$. Equation 12 gives the relation between the inelastic strain-rate tensor $\dot{\boldsymbol{\varepsilon}}^{\text{in}}$ and the stress deviator, $\mathbf{s}$, in which σ_0 denotes the scalar static yield stress, below which no inelastic deformation occurs (the expression between brackets is set to 0 when it is negative). In these equations, the temperature dependency of all the involved variables should be considered. The effect of strain hardening may appear in such a model by the increase of both the static yield stress σ_0 and the plastic consistency K with the accumulated inelastic strain ε_{eq}, or with another state variable that is representative of the material structure. The corresponding scalar equation relating stress and inelastic strain-rate von Mises invariants is:

$$\sigma_{\text{eq}} = \sigma_0 + K(\dot{\varepsilon}_{\text{eq}})^m \qquad \text{(Eq 14)}$$

Inserting this into Eq 12 simplifies it to:

$$\dot{\boldsymbol{\varepsilon}}^{\text{in}} = \frac{3\dot{\varepsilon}_{\text{eq}}}{2\sigma_{\text{eq}}}\mathbf{s}, \text{ or, in incremental form, } d\boldsymbol{\varepsilon}^{\text{in}} = \frac{3d\varepsilon_{\text{eq}}}{2\sigma_{\text{eq}}}\mathbf{s} \qquad \text{(Eq 15)}$$

Although metallic alloys show a significant strain-rate sensitivity at high temperature, they are often modeled in the literature using elastic-plastic models, neglecting this important effect. In this case, Eq 15 still holds, but the flow stress is independent of the strain rate. It may depend on the accumulated plastic strain because of strain hardening.

Implementation Issues. One of the major difficulties in the thermomechanical analysis of casting processes is the concurrent presence of liquid, mushy, and solid regions that move with time as solidification progresses. Several different strategies have been developed, according to the process and model objectives:

- A first strategy consists in extracting the solidified regions of the casting domain based on the thermal analysis results. Then, a small-strain thermomechanical analysis is carried out on just this solid subdomain, using a standard solid-state constitutive model. Besides difficulties with the extraction process, especially when the solidified regions have complex unconnected shapes, this method may have numerical problems with the application of the liquid hydrostatic pressure onto the new internal boundary of the solidified region. However, this simple strategy is very convenient for many practical problems, especially when the solidification front is stationary, such as the primary cooling of continuous casting of aluminum (Ref 12) and steel (Ref 13, 14). For transient problems, such as the prediction of residual stress and shape (butt-curl) during startup of the aluminum direct chill continuous casting process, the domain can be extended in time by adding layers (Ref 12).
- A second strategy considers the entire casting, including the mushy, and liquid regions. The liquid, mushy, and solid regions are modeled as a continuum by adopting the constitutive equations for the solid phase (see the previous section "Solid-State Constitutive Models") for all regions by adjusting material parameters such as K, m, E, ν, σ_0, and ρ according to temperature. For example, liquid can be treated by setting the strains to 0 when the temperature is above the solidus temperature. This ensures that stress development in the liquid phase is suppressed. In the equilibrium equation, Eq 2, acceleration terms are neglected, and a small-strain analysis can be performed. The primary unknowns are the displacements, or displacement increments. This popular approach can be used with structural finite element codes, such as MARC (Ref 15) or ABAQUS (Ref 16), and with

commercial solidification codes or special-purpose software, such as ALSIM (Ref 17)/ ALSPEN, (Ref 18), CASTS, (Ref 19), CON2D (Ref 20, 21), Magmasoft (Ref 22), and Procast (Ref 23, 24). It has been applied successfully to simulate deformation and residual stress in shape castings (Ref 25, 26), direct chill casting of aluminum (Ref 12, 17, 18, 27–29), and continuous casting of steel (Ref 20, 30). Despite its efficiency, this approach may suffer from several drawbacks. First, it cannot properly account for fluid flow and the volumetric shrinkage that affects flow in the liquid pool, fluid feeding into the mushy zone, and primary shrinkage depressions that affect casting shape. In addition, incompressibility of the metal in the liquid state is accounted for by increasing Poisson's ratio to close to 0.5 which sometimes makes the solution prone to numerical instability (Ref 31, 32).

- A third strategy has recently been developed that addresses the above issues. It still simulates the entire casting, but treats the mass and momentum equations of the liquid and mushy regions with a mixed velocity-pressure formulation. The primary unknowns are the velocity (time derivative of displacement) and pressure fields, which make it easier to impose the incompressibility constraint (see next section "Thermomechanical Coupling"). Indeed, the velocity-pressure formulation is also applied to the equilibrium of the solid regions to provide a single continuum framework for the global numerical solution. This strategy has been implemented into codes dedicated to casting analysis such as THERCAST (Ref 30, 33, 34) and VULCAN (Ref 35). If stress prediction is not important so that elastic strains can be ignored, then this formulation simplifies to a standard fluid-flow analysis, which is useful in the prediction of bulging and shape in large-strain processes.

Example of Solid-State Constitutive Equations. Material property data are needed for the specific alloy being modeled and in a form suitable for the constitutive equations just discussed. This presents a significant challenge for quantitative mechanical analysis, because measurements are not presented in this form and only rarely supply enough information on the conditions to allow transformation to an alternate form. As an example, the following elastic-viscoplastic constitutive equation was developed for the austenite phase of steel (Ref 36) by fitting constant strain-rate tensile tests (Ref 37, 38) and constant-load creep tests (Ref 39) to the form required in Eq 10 to Eq 13.

$$\dot{\varepsilon}_{eq} = f_{\%C}\langle \sigma_{eq} - \sigma_0 \rangle^{1/m} \exp\left(-\frac{4.465 \times 10^4}{T}\right) \quad \text{(Eq 16)}$$

where

$f_{\%C} = 4.655 \times 10^4 + 7.14 \times 10(\%C) + 1.2 \times 10^4(\%C)^2$

$\sigma_0 = (130.5 - 5.128 \times 10^{-3}T)\varepsilon_{eq}{}^{f_2}$

$f_2 = -0.6289 + 1.114 \times 10^{-3}T$

$1/m = 8.132 - 1.54 \times 10^{-3}T$

with T[K]. σ_{eq}. σ_0[MPa]

This equation, and a similar one for delta ferrite, have been implemented into the finite-element codes CON2D (Ref 20) and THERCAST (Ref 40) and applied to investigate several problems involving mechanical behavior during continuous casting.

Elastic modulus is a crucial property that decreases with increasing temperature. It is difficult to measure at the high temperatures important to casting, owing to the susceptibility of the material to creep and thermal strain during a standard tensile test, which results in excessively low values. Higher values are obtained from high strain-rate tests, such as ultrasonic measurements (Ref 41) Elastic modulus measurements in steels near the solidus temperature range from ~1 GPa (145 ksi) (Ref 42) to 44 GPa (6400 ksi) (Ref 43) with typical modulus values ~10 GPa (1450 ksi) near the solidus (Ref 44–46).

The density needed to compute thermal strain in Eq 4, 8, or 13 can be found from a weighted average of the values of the different solid and liquid phases, based on the local phase fractions. For the example of plain low-carbon steel, the following equations were compiled (Ref 20) based on solid data for ferrite (α), austenite (γ), and delta (δ) (Ref 47, 48) and liquid (l) measurements (Ref 49).

$$\begin{aligned}\rho(\mathrm{kg/m^3}) &= \rho_\alpha f_\alpha + \rho_\gamma f_\gamma + \rho_\delta f_\delta + \rho_l f_l \\ \rho_\alpha &= 7881 - 0.324\mathrm{T}(^\circ\mathrm{C}) - 3 \times 10^{-5}T(^\circ\mathrm{C})^2 \\ \rho_\gamma &= \frac{100[8106 - 0.51T(^\circ\mathrm{C})]}{[100 - (\%\mathrm{C})][1 + 0.008(\%\mathrm{C})]^3} \\ \rho_\delta &= \frac{100[8011 - 0.47T(^\circ\mathrm{C})]}{[100 - (\%\mathrm{C})][1 + 0.013(\%\mathrm{C})]^3} \\ \rho_l &= 7100 - 73(\%\mathrm{C}) - [0.8 - 0.09(\%\mathrm{C})] \\ &\quad [T(^\circ\mathrm{C}) - 1550] \end{aligned} \quad \text{(Eq 17)}$$

Specialized experiments to measure mechanical properties for use in computational models will be an important trend for future research in this field.

Thermomechanical Coupling

Coupling between the thermal and mechanical analyses arises from several sources. First, regarding the mechanical problem, besides the strain rate due to thermal expansion and solidification shrinkage, the material parameters of the preceding constitutive equations strongly depend on temperature and phase fractions, as shown in the previous section. Second, in the heat-transfer problem, the thermal exchange between the casting and the mold strongly depends on local conditions such as the contact pressure or the presence of a gap between them (as a result of thermal expansion and solidification shrinkage). This is illustrated in Fig. 1 and discussed in this section.

Air Gap Formation: Conductive-Radiative Modeling. In the presence of a gap between the casting and the mold, resulting from their relative deformation, the heat transfer results from concurrent conduction through the gas within the gap and from radiation. The exchanged thermal flux, q_{gap}, can then be written:

$$q_{gap} = \frac{k_{gas}}{g}(T_c - T_m) + \frac{\sigma(T_c^4 - T_m^4)}{\frac{1}{\varepsilon_c} + \frac{1}{\varepsilon_m} - 1} \quad \text{(Eq 18)}$$

with k_{gas} (T) the thermal conductivity of the gas, g the gap thickness, T_c and T_m the local surface temperature of the casting and mold, respectively, ε_c and ε_m their gray-body emissivities, σ the Stefan-Boltzmann constant. It is to be noted that the conductive part of the flux can be written in more detail to take into account the presence of coating layers on the mold surface: conduction through a medium of thickness g_{coat}, of conductivity k_{coat} (T). It can be seen that the first term tends to infinity as the gap thickness tends to 0; this expresses a perfect contact condition, T_c and T_m tending toward a unique interface temperature. The reality is somewhat different, showing always nonperfect contact conditions. Therefore, the conductive heat-exchange coefficient $h_{cond} = k_{gas}/g$ should be limited by a finite value h_0, corresponding to the "no-gap" situation, and depends on the roughness of the casting surface. Specific examples of these gap heat-transfer laws are provided elsewhere for continuous casting with oil lubrication (Ref 13) and mold flux (Ref 50).

Effective Contact: Heat Transfer as a Function of Contact Pressure. With effective contact, the conductive heat flux increases with the contact pressure according to a power law (Ref 51). Still denoting h_0 as the heat-exchange coefficient corresponding to no gap and no contact pressure, the interfacial heat flux is:

$$q_{contact} = (h_0 + Ap_c^B)(T_c - T_m) \quad \text{(Eq 19)}$$

with p_c the contact pressure, A and B two parameters that depend on the materials, the presence of coating or lubricating agent, the surface roughness, and the temperature. The parameters and possibly the laws governing their evolution need to be determined experimentally.

Numerical Solution

The thermomechanical modeling equations just presented must be solved numerically, owing to the complex shape of the casting process domain, and the highly nonlinear material properties. The calculation depends greatly on the numerical resolution of time and space. Although finite-difference approaches are

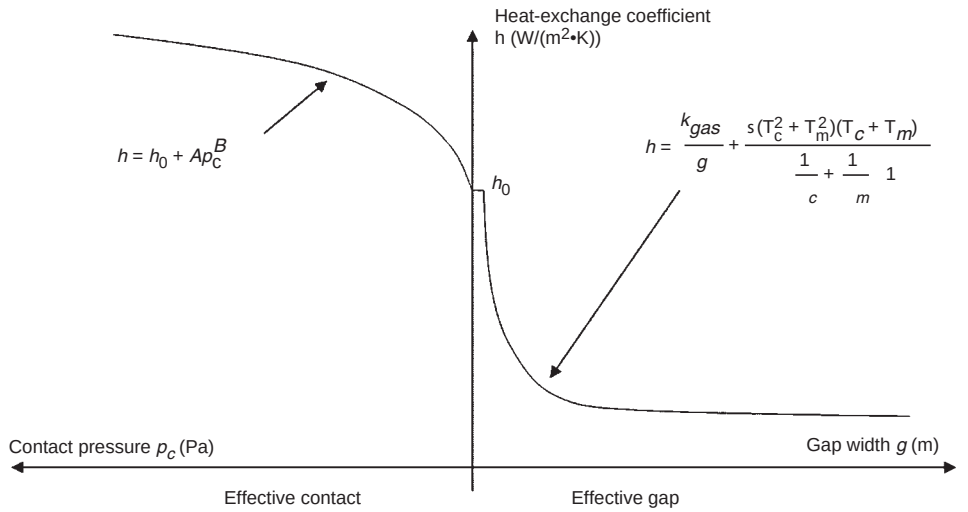

Fig. 1 Modeling of the local heat transfer coefficient in the gap and effective contact situations

popular for heat-transfer, solidification, and fluid-flow analyses, the finite element formulation is usually preferred for the mechanical analysis, owing to its historical advantages with unstructured meshes and accurate implicit solution of the resulting simultaneous algebraic equations. The latter are discussed below.

Finite Element Formulation and Numerical Implementation

In the framework of the small-strain approach presented previously (see the section "Implementation Issues"), having displacements for primitive unknowns, the weak form of the equilibrium equation, Eq 2, neglecting inertia terms, is written as:

$$\forall \mathbf{u}^* \quad \int_\Omega \boldsymbol{\sigma} : d\boldsymbol{\varepsilon}(\mathbf{u}^*) dV - \int_{\partial\Omega} \mathbf{T} \cdot \mathbf{u}^* dS - \int_\Omega \rho \mathbf{g} \cdot \mathbf{u}^* dV = 0 \qquad \text{(Eq 20)}$$

where $\mathbf{T}$ is the external stress vector. The vector test functions $\mathbf{u}^*$ can be seen as virtual displacements in a statement of virtual work.

If the third strategy described in the section "Implementation Issues" is adopted, with velocity and pressure as primary unknown variables, the weak form of the momentum equation (Eq 2) is written as (Ref 52):

$$\begin{cases} \forall \mathbf{v}^* & \displaystyle\int_\Omega \mathbf{s} : \dot{\boldsymbol{\varepsilon}}(\mathbf{v}^*) dV - \int_\Omega p \nabla \cdot \mathbf{v}^* dV - \int_{\partial\Omega} \mathbf{T} \cdot \mathbf{v}^* dS - \int_\Omega \rho \mathbf{g} \cdot \mathbf{v}^* dV + \int_\Omega \rho \frac{d\mathbf{v}}{dt} \cdot \mathbf{v}^* dV = 0 \\ \forall p^* & \displaystyle\int_\Omega p^* tr(\dot{\boldsymbol{\varepsilon}}^{\text{in}}) dV = 0 \end{cases} \qquad \text{(Eq 21)}$$

The first equation contains vector test functions $\mathbf{v}^*$, which can be seen as virtual velocities in a statement of virtual power. Unlike Eq 20, the pressure p is a primary variable, and only the deviatoric part of the constitutive equations is involved (to determine the stress deviator $\mathbf{s}$). This is why the second equation is needed, which consists of a weak form of the incompressibility of inelastic deformations.

Equations 20 and 21 are spatially discretized using the standard finite-element method, as explained in detail in many references (Ref 52). Combined with time discretization using finite differences, this leads to a set of nonlinear equations to be solved at each time increment. In the context of the displacement strategy, Eq 20, this leads to:

$$\mathbf{R}(\mathbf{U}) = 0 \qquad \text{(Eq 22)}$$

where $\mathbf{R}$ is the vector of the nodal equilibrium residues (number of components: 3 × number of nodes, in three dimensions), and $\mathbf{U}$ is the vector of nodal incremental displacements (same size).

Adopting the velocity-pressure strategy, Eq 21 leads to a set of nonlinear equations:

$$\mathbf{R}'(\mathbf{V}, \mathbf{P}) = 0 \qquad \text{(Eq 23)}$$

where $\mathbf{R}'$ is the vector of the nodal residues (number of components: 4 × number of nodes, in dimension 3), $\mathbf{V}$ is the vector of nodal velocities (size: 3 × number of nodes), and $\mathbf{P}$ is the vector of nodal pressures (size: number of nodes).

The global finite-element systems Eq 22 or Eq 23 are usually solved using a full or modified Newton-Raphson method (Ref 16, 31), which iterates to minimize the norm of the residue vectors $\mathbf{R}$ or $\mathbf{R}'$. Alternatively, explicit methods may be employed at this global level.

At the local (finite element) level, an algorithm is also required to integrate the constitutive equations, when they depend on strain rate or strain. When the constitutive equations are highly nonlinear, an implicit algorithm is useful to perform time integration at each Gauss point to provide better estimates of inelastic strain at the local level (Ref 53–55).

Boundary Conditions: Modeling of Contact Conditions. Multidomain Approaches

At the interface between the solidifying material and the mold, a contact condition is required to prevent penetration of the shell into the mold, while allowing shrinkage of the shell away from the mold to create an interfacial gap:

$$\begin{cases} \boldsymbol{\sigma}\,\mathbf{n} \cdot \mathbf{n} \le 0 \\ g \ge 0 \\ (\boldsymbol{\sigma}\,\mathbf{n} \cdot \mathbf{n})\mathrm{g} = 0 \end{cases} \qquad \text{(Eq 24)}$$

where g is the local interface gap width (positive when air gap exists effectively, as in section 0) and $\mathbf{n}$ is the local outward unit normal to the part. Equation 24 can be satisfied with a penalty condition, which consists of applying a normal stress vector $\mathbf{T}$ proportional to the penetration depth (if any) via a penalty constant χ_p:

$$\mathbf{T} = \boldsymbol{\sigma}\,\mathbf{n} = -\chi_p \langle -g \rangle \mathbf{n} \qquad \text{(Eq 25)}$$

Here again, the brackets denote the positive part; a repulsive stress is applied only if g is negative (penetration). Different methods of local adaptation of the penalty coefficient χ_p have been developed, including the augmented Lagrangian method (Ref 56). More complex and computationally expensive methods, such as the use of Lagrange multipliers may also be used (Ref 57).

The possible tangential friction effects between part and mold can be taken into account by a friction law, such as a Coulomb model for instance. In this case, the previous stress vector has a tangential component, $\mathbf{T}_\tau$, given by:

$$\mathbf{T}_\tau = -\mu_f p_c \frac{1}{\|\mathbf{v} - \mathbf{v}_{\text{mold}}\|} (\mathbf{v} - \mathbf{v}_{\text{mold}}) \qquad \text{(Eq 26)}$$

where $p_c = -\sigma_n = -\boldsymbol{\sigma}\mathbf{n} \cdot \mathbf{n}$ is the contact pressure, and μ_f the friction coefficient.

The previous approach can be extended to the multidomain context to account for the deformation of mold components. The local stress vectors calculated by Eq 25 can be applied onto the surface of the mold, contributing then to its deformation. For most casting processes, the mechanical interaction between the cast product and the mold is sufficiently slow (i.e., its characteristic time remains significant with respect to the process time) to permit a staggered scheme within each time increment: the mechanical problem is successively solved in the cast product and in the different mold components. A global updating of the different configurations is then performed at the end of the time

increment. This simple approach gives access to a prediction of the local air gap size g, or alternatively of the local contact pressure p_c, that is used in the expressions of the heat-transfer coefficient, according to Eq 18 and 19 (Ref 58).

Treatment of the Regions in the Solid, Mushy, and Liquid States

Solidified Regions: Lagrangian Formulation. In casting processes, the solidified regions generally encounter small deformations. It is thus natural to embed the finite element domain into the material, with each node of the computational grid corresponding with the same solid particle during its displacement. The boundary of the mesh corresponds then to the surface of the casting. This method, called Lagrangian formulation, provides the best accuracy when computing the gap forming between the solidified material and the mold. It is also the more reliable and convenient method for time integration of highly nonlinear constitutive equations, such as elastic-(visco)plastic laws presented in the section "Solid-State Constitutive Models."

Mushy and liquid regions: ALE modeling. When the mushy and liquid regions are modeled in the same domain as the solid (see the discussion in the section "Implementation Issues"), they are often subjected to large displacements and strains arising from solidification shrinkage, buoyancy, or forced convection. Similar difficulties are generated in casting processes such as squeeze casting, where the entire domain is highly deformed. In these cases, a Lagrangian formulation would demand frequent remeshings to avoid mesh degeneracy, which is both computationally costly and detrimental to the accuracy of the modeling. It is then preferable to use a so-called Arbitrary Lagrangian Eulerian formulation (ALE). In a Eulerian formulation, material moves through the computational grid, which remains stationary in the "laboratory" frame of reference. In the ALE formulation, the updating of the mesh is partially independent of the velocity of the material particles to maintain the quality of the computational grid. Several methods can be used, including the popular "barycentering" technique, which keeps each node at the geometrical centroid of a set of its neighbors. This method involves significant extra complexity to account for the advection of material through the domain, and the state variables such as temperature and inelastic strain must be updated according to the relative velocity between the mesh and the particles. In doing this, some surface constraints must be enforced to ensure mass conservation, expressing that the fluxes of mesh velocity and of fluid particle velocity through the surface of the mesh should remain identical. A review on the ALE method in solidification modeling is available, together with some details on its application (Ref 33).

Thermomechanical Coupling

Because of the interdependency of the thermal and mechanical analyses, as presented in the section "Thermomechanical Coupling," their coupling should be taken into account all throughout the cooling process. In practice, the cooling time is decomposed into time increments, each increment requiring the solution of two problems: the energy conservation and the momentum conservation. With the highly nonlinear elastic-viscoplastic constitutive equations typical of solidifying metals, the incremental steps required for the mechanical analysis to converge are generally much smaller than those for the thermal analysis. Thus, these two analyses are generally performed in succession and only once per time increment. However, in the case of very rapid cooling, these solutions might preferably be performed together (including thermal and mechanical unknowns in a single set of nonlinear equations), or else separately but iteratively until convergence at each time increment, otherwise the time step has to be dramatically reduced.

Model Validation

Model validation with both analytical solutions and experiments is a crucial step in any computational analysis, and thermomechanical modeling is no exception. Weiner and Boley (Ref 59) derived an analytical solution for unidirectional solidification of an unconstrained plate with a unique solidification temperature, an elastic perfectly plastic constitutive law and constant properties. The plate is subjected to sudden surface quench from a uniform initial temperature to a constant mold temperature.

This benchmark problem is ideal for estimating the discretization errors of computational thermal-stress models, as it can be solved with a simple mesh consisting of one row elements, as shown in Fig. 2. Numerical predictions should match with acceptable precision using the same element type and mesh refinement planned for the real problem. For example, the solidification stress analysis code, CON2D (Ref 20) and the commercial code ABAQUS were applied for typical conditions of steel casting (Ref 21).

Figures 3 and 4 compare the temperature and stress profiles in the plate at two times. The temperature profile through the solidifying shell is almost linear. Because the interior cools relative to the fixed surface temperature, its shrinkage generates internal tensile stress, which induces compressive stress at the surface. With no applied external pressure, the average stress through the thickness must naturally equal 0, and stress must decrease to 0 in the liquid. Stresses and strains in both transverse directions are equal for this symmetrical problem. The close agreement demonstrates that both computational models are numerically

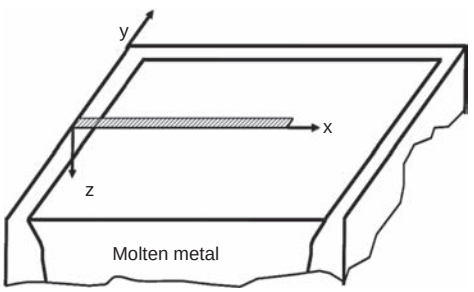

Fig. 2 One-dimensional slice domain for modeling solidifying plate

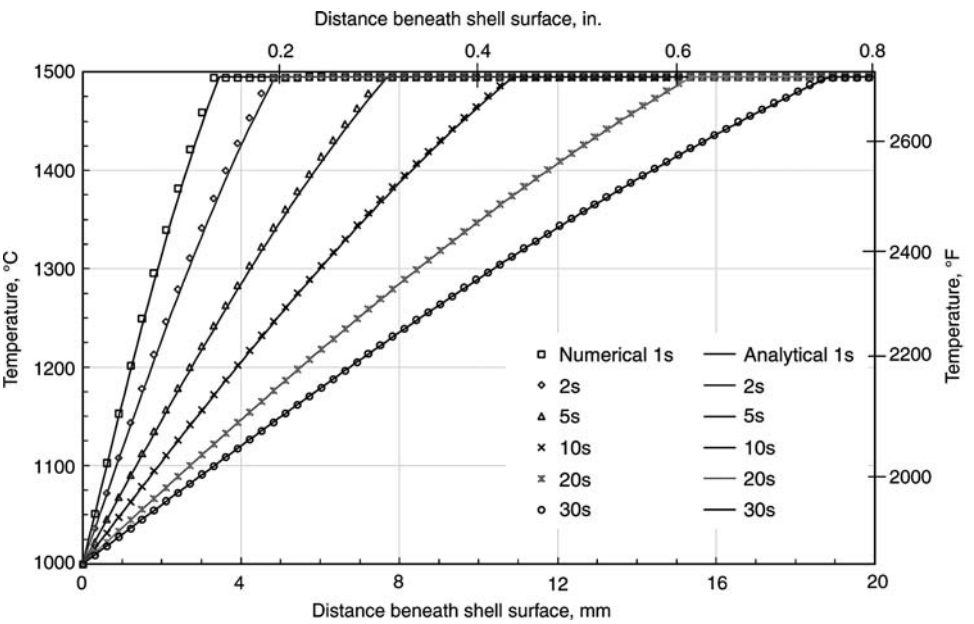

Fig. 3 Temperatures through solidifying plate at different times comparing analytical solution and numerical predictions

consistent and have an acceptable mesh resolution. Comparison with experimental measurements is also required to validate that the modeling assumptions and input data are reasonable.

Example Applications

Sand Casting of Braking Disks. The finite element software THERCAST for thermomechanical analysis of solidification (Ref 34) has been used in the automotive industry to predict distortion of gray-iron braking discs cast in sand molds (Ref 60). Particular attention has been paid to the interaction between the deformation of internal sand cores and the cast parts. This demands a global coupled thermomechanical simulation, as presented previously. Figure 5 illustrates the discretization of the different domains involved in the calculation. The actual cooling scenario has been simulated: cooling in mold for 45 min, shakeout, and air cooling for 15 min. Figure 6 shows the temperature evolution at different points in a horizontal cross section at midheight in the disc, revealing: solidification after 2 min, and solid-state phase change after 20 min. The calculated deformation of the core blades shows thermal buckling caused by the very high temperature, and constraint of their dilatation, as shown in Fig. 7. This deformation causes a difference in thickness between the two braking tracks of the disc. Such a defect needs heavy and costly machining operations to produce quality parts. Instead, process simulation allows the manufacturer to test alternative geometries and process conditions in order to minimize the defect.

Similar thermomechanical calculations have been made for plain discs, leading to comparisons with residual stress measurements by means of neutrons and x-ray diffraction (Ref 61). As shown in Fig. 8, calculations are consistent with measurements to within 10 MPa (1.5 ksi).

Continuous Casting of Steel Slabs. Thermomechanical simulations are used by steelmakers to analyze stresses and strains both in the mold and in the secondary cooling zone below. One goal is to quantify the bulging of the solidified crust between the supporting rolls that is responsible for the tensile stress state in the mushy core, which in turn induces internal cracks and macrosegregation (Ref 62, 63). Two- and three-dimensional finite element models have been recently developed, for the entire length of the caster using THERCAST, as described elsewhere (Ref 40, 64). The constitutive models were presented in the section "Governing Equations." Contact with supporting rolls is simulated with the penalty formulation discussed in the section "Boundary Conditions: Modeling of Contact Conditions. Multidomain Approaches" adapting penalty coefficients for the different rolls continuously to control numerical penetration of the strand.

Figure 9 shows results for a vertical-curved machine (strand thickness 0.22 m, or 0.75 ft, casting speed 0.9 m/min, or 3 ft/min, material Fe-0.06wt%C) at around 11 m (36 ft) below the meniscus. The pressure distribution reveals a double alternation of compressive and

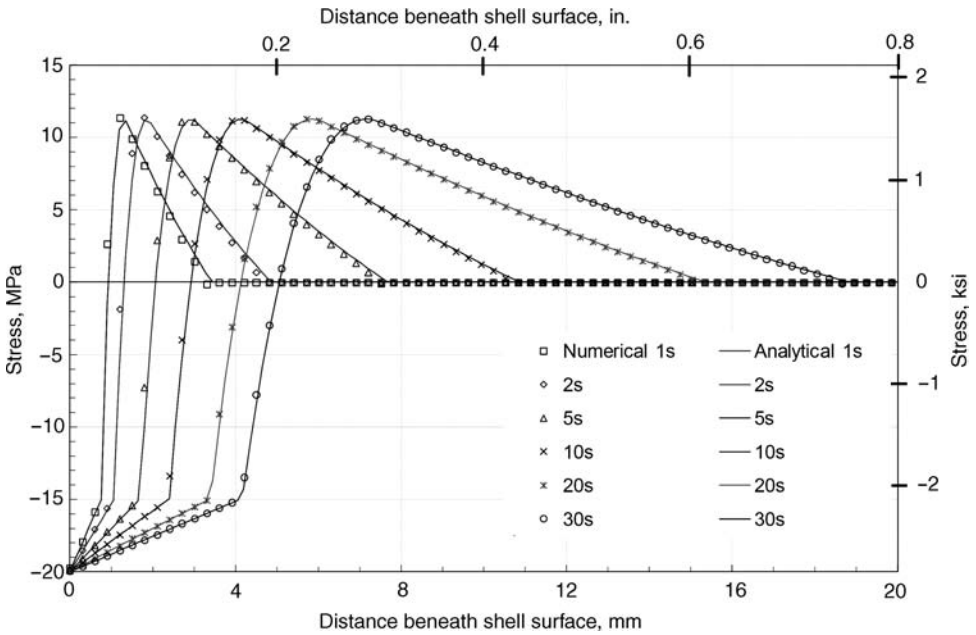

Fig. 4 Transverse (*Y* and *Z*) stress through solidifying plate at different times comparing analytical solution and numerical predictions

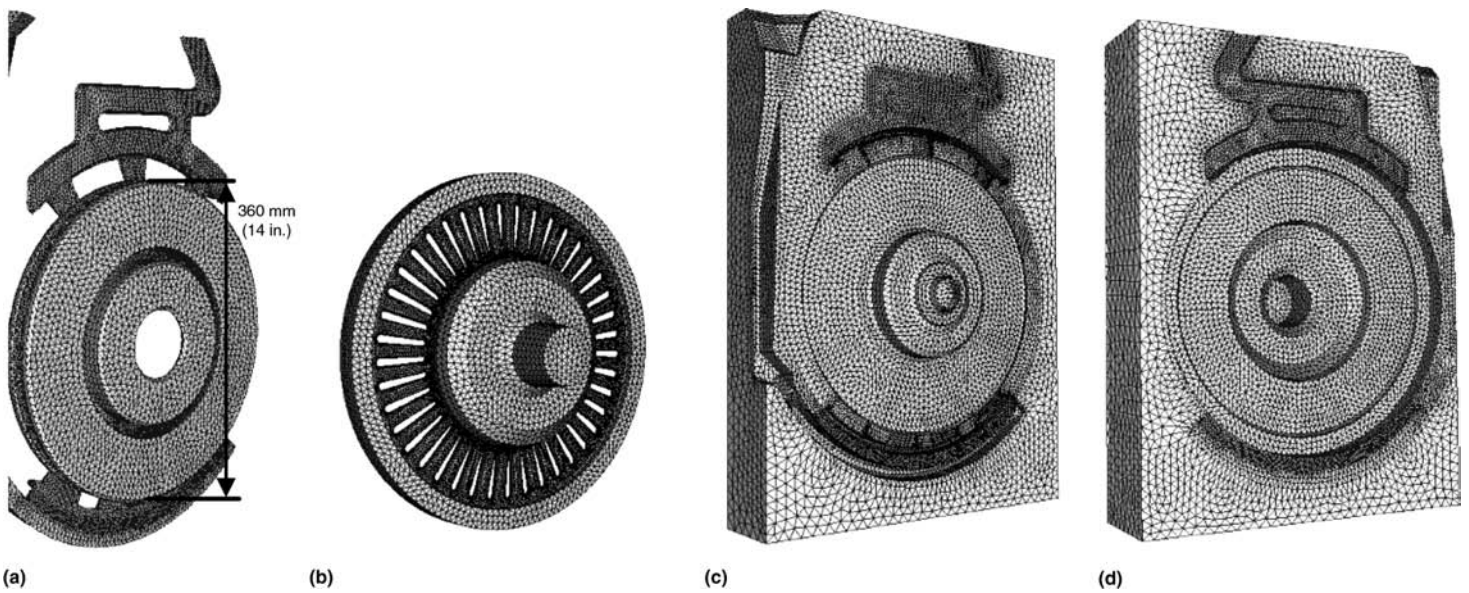

Fig. 5 Finite element meshes of the different domains: part, core, and two half molds

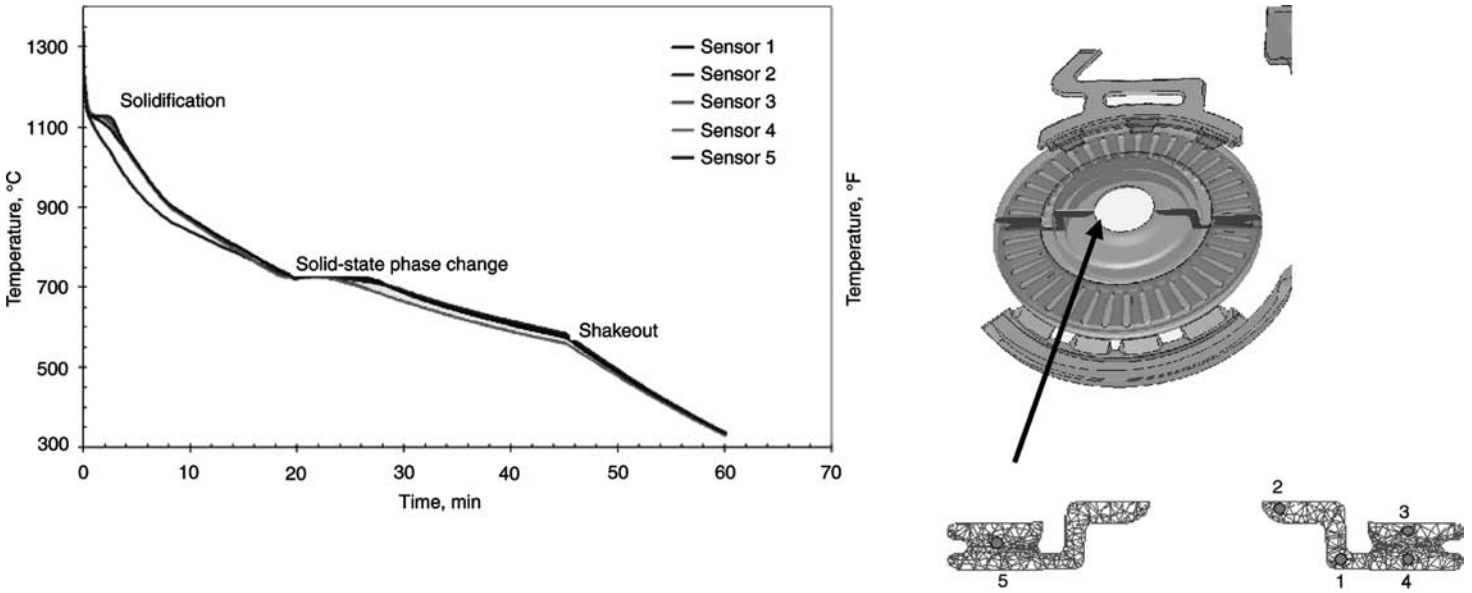

Fig. 6 Temperature evolution in the part at different points located in the indicated section

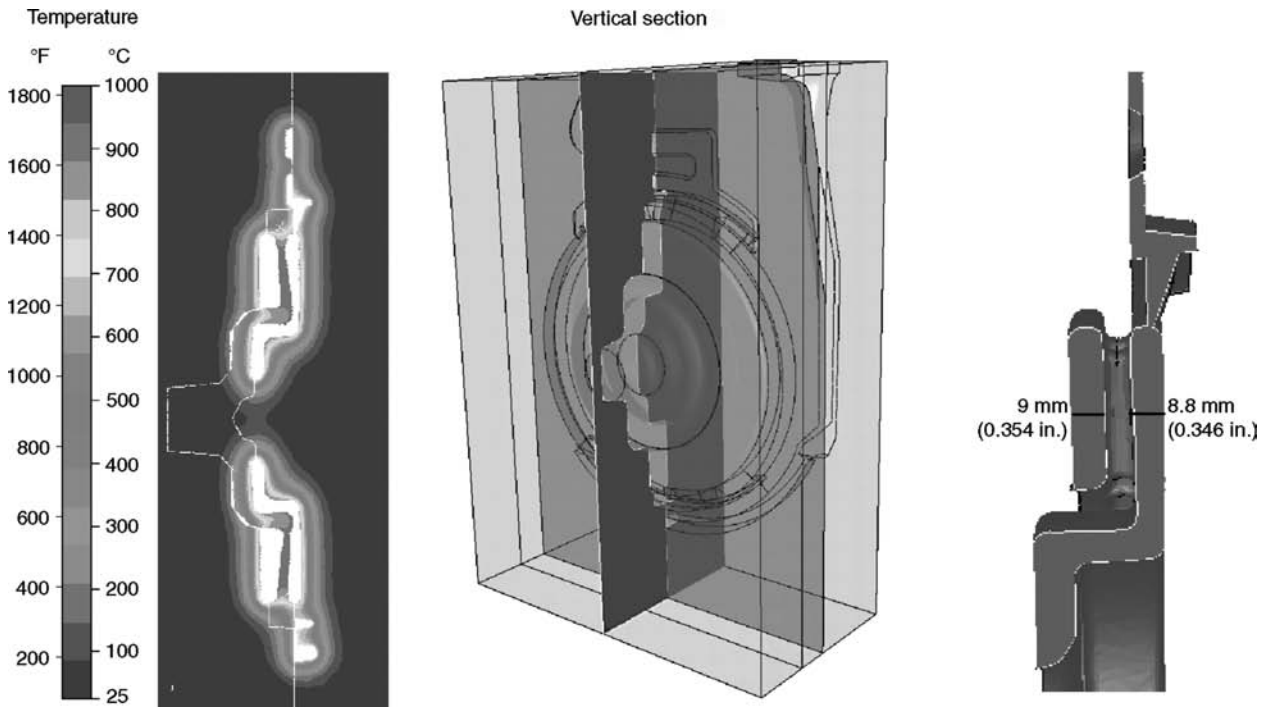

Fig. 7 Deformation of core blades in a radial section, after a few seconds of cooling. On the left, displacements are magnified (100×). The temperature distribution is superimposed. On the right, the difference in thickness between the two braking tracks is shown.

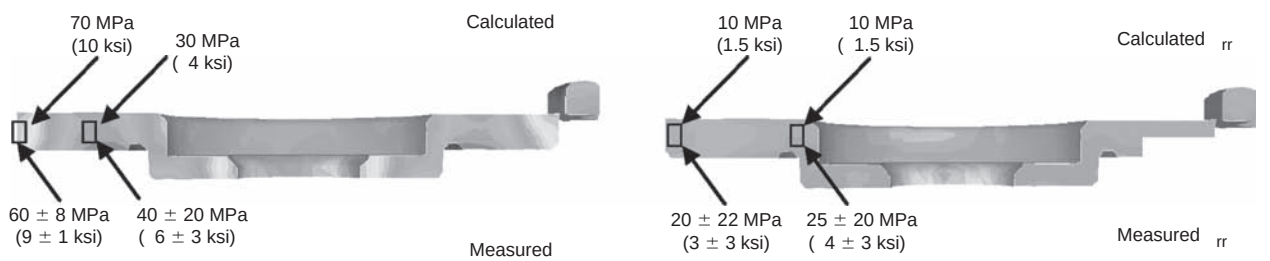

Fig. 8 Residual hoop stresses (left) and radial stresses (right) in a radial section on as-cast plain discs made of gray iron. Top line, calculated values; bottom line, measured values

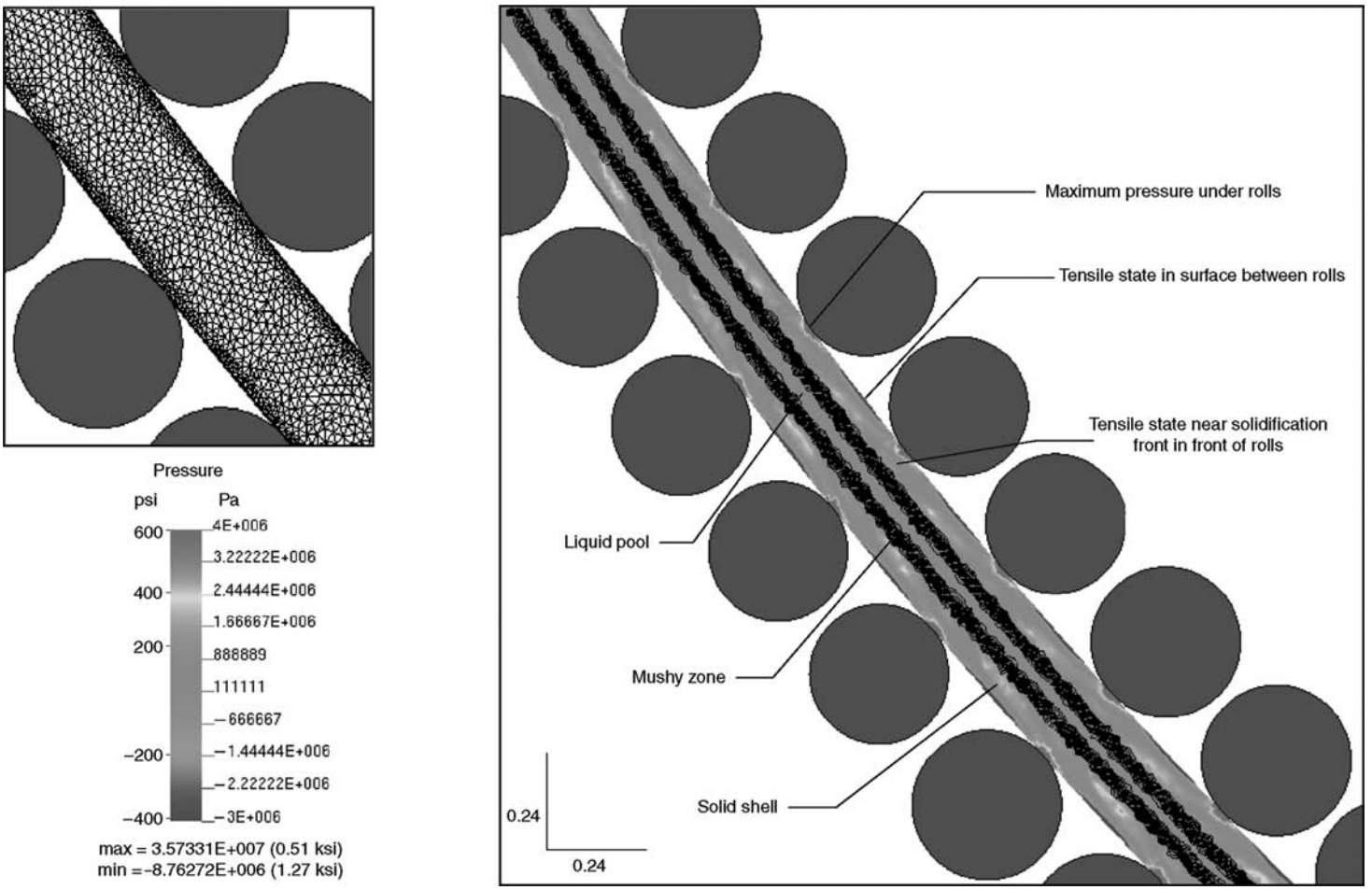

Fig. 9 Predictions in the middle of the secondary cooling zone, about 11 m (36 ft) below the meniscus. The finite element mesh, (top left) features a fine band of 20 mm (0.8 in.). The pressure distribution (right) reveals alternating stress, including tension near the solidification front (the mushy zone is materialized by 20 lines separated by an interval $\Delta g_l = 0.05$).

depressive zones. First, the strand surface is in a compressive state under the rolls where the pressure reaches its maximum, 36 MPa (5 ksi). Conversely, it is in a depressive (tensile) state between rolls, where the pressure is minimum (−9 MPa, or −1 ksi). Near the solidification front (i.e., close to the solidus isotherm), the stress alternates between tension (negative pressure of about −2 MPa, or −0.3 ksi) beneath the rolls and compression in between (2–3 MPa, or 0.3–0.4 ksi). These results agree with previous structural analyses of the deformation of the solidified shell between rolls, such as those carried out in static conditions by Wünnenberg and Huchingen (Ref 65), Miyazawa and Schwerdtfeger (Ref 62), or by Kajitani et al. (Ref 66) on small slab sections moving downstream between rolls and submitted to the metallurgical pressure onto the solidification front.

The influence of process parameters on the thermomechanical state of the strand can then be studied using such numerical models. An example is given in Fig. 10, presenting the sensitivity of bulging to the casting speed. It can also be seen that bulging predictions are sensitive to the roll pitch, a larger pitch between two sets of rolls inducing an increased bulging. These numerical simulations can then be used to study possible modifications in the design of continuous casters, such as the replacement of large rolls by smaller ones to reduce the pitch and the associated bulging (Ref 67).

Hot-Tearing Analysis

Hot-tear crack formation is one of the most important consequences of stress during solidification. Hot tearing is caused by a combination of tensile stress and metallurgical embrittlement. It occurs at temperatures near the solidus when strain concentrates within the interdendritic liquid films, causing separation of the dendrites and intergranular cracks at very small strains (on the order of 1%). This complex phenomenon depends on the ability of liquid to flow through the dendritic structure to feed the volumetric shrinkage, the strength of the surrounding dendritic skeleton, the grain size and shape, the nucleation of supersaturated gas into pores or crack surfaces, the segregation of solute impurities, and the formation of interfering solid precipitates. The subsequent refilling of hot tears with segregated liquid alloy can cause internal defects that are just as serious as exposed surface cracks. The hot tearing of aluminum alloys is reviewed elsewhere (Ref 68). Hot-tearing phenomena are too complex, too small-scale, and insufficiently understood to model in detail, so several different criteria have been developed to predict hot tears from the results of a thermomechanical analysis.

Thermal Analysis Criteria. Casting conditions that produce faster solidification and alloys with wider freezing ranges are more prone to hot tears. Thus, many criteria are solely based on thermal analysis. Clyne and Davies simply compare the local time spent between two critical solid fractions g_{s1} and g_{s2} (typically 0.9 and 0.99, respectively), with the total local solidification time (or a reference solidification time) (Ref 69). The "hot-cracking susceptibility" is defined as:

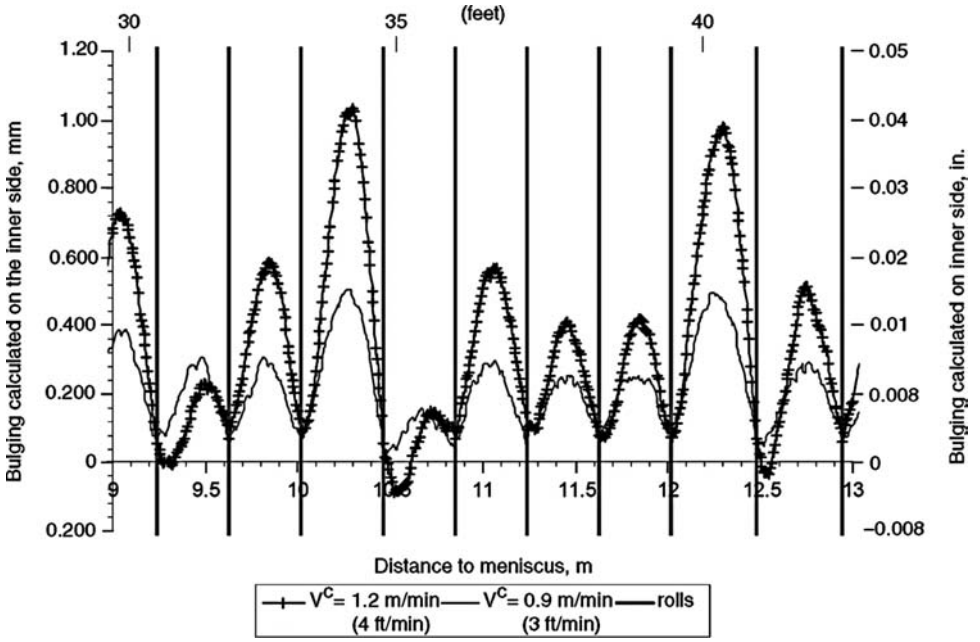

Fig. 10 Slab bulging calculated at two different casting speeds: 0.9 and 1.2 m/min (3 and 4 ft/min). The slab bulging increases with the casting speed. Source: Ref 67

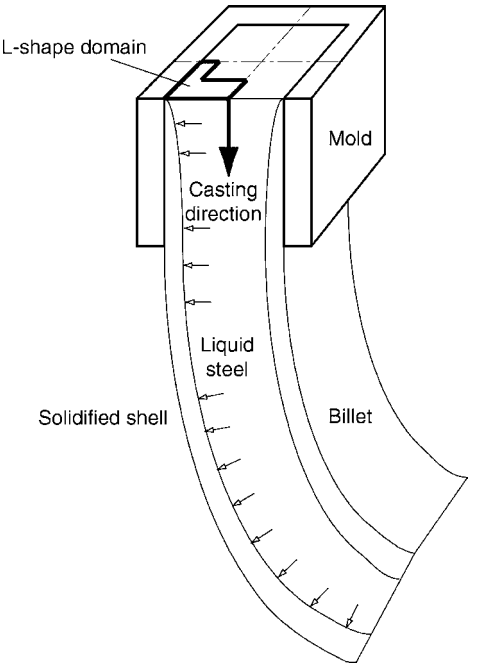

Fig. 11 Model domain

$$HCS_{\text{Clyne}} = \frac{t_{0.99} - t_{0.90}}{t_{0.90} - t_{0.40}} \quad \text{(Eq 27)}$$

Classical Mechanics Criteria. Criteria based on classical mechanics often assume cracks will form when a critical stress is exceeded, and they are popular for predicting cracks at lower temperatures (Ref 70–73). This critical stress depends greatly on the local temperature and strain rate. Its accuracy relies on measurements, such as the submerged split-chill tensile test for hot tearing (Ref 74–76).

Measurements often correlate hot-tear formation with the accumulation of a critical level of mechanical strain while applying tensile loading within a critical solid fraction where liquid feeding is difficult. This has formed the basis for many hot-tearing criteria. That of Yamanaka et al. (Ref 77) accumulates inelastic deformation over a brittleness temperature range, which is defined, for example as $g_s \in [0.85, 0.99]$ for a Fe-0.15wt%C steel grade. The local condition for fracture initiation is then:

$$\sum_{g_{s1}}^{g_{s2}} \Delta\varepsilon^{\text{in}} \geq \varepsilon_{\text{cr}} \quad \text{(Eq 28)}$$

in which the critical strain ε_{cr} is 1.6% at a typical strain rate of 3×10^{-4} s^{-1}. Careful measurements during bending of solidifying steel ingots have revealed critical strains ranging from 1 to 3.8% (Ref 77, 78). The lowest values were found at high strain rate and in crack-sensitive grades (e.g., high-sulfur peritectic steel) (Ref 77). In aluminum-rich Al-Cu alloys, critical strains were reported from 0.09 to 1.6% and were relatively independent of strain rate (Ref 79). Tensile stress is also a requirement for hot-tear formation (Ref 77). The maximum tensile stress occurs just before formation of a critical flaw (Ref 79).

The critical strain decreases with increasing strain rate, presumably because less time is available for liquid feeding, and also decreases for alloys with wider freezing ranges. Won et al. (Ref 80) suggested the following empirical equation for the critical strain in steel, based on fitting measurements from many bend tests:

$$\varepsilon_{\text{cr}} = \frac{0.02821}{\dot{\varepsilon}^{0.3131} \Delta T_{\text{B}}^{0.8638}} \quad \text{(Eq 29)}$$

where $\dot{\varepsilon}$ is the strain rate and ΔT_{B} is the brittle temperature range, defined between the temperatures corresponding to solid fractions of 0.9 and 0.99.

Mechanistically Based Criteria. More mechanistically based hot-tearing criteria include more of the local physical phenomena that give rise to hot tears. Feurer (Ref 81) and more recently Rappaz et al. (Ref 82) have proposed that hot tears form when the local interdendritic liquid feeding rate is not sufficient to balance the rate of tensile strain increase across the mushy zone. The criterion of Rappaz et al. predicts fracture when the strain rate exceeds a limit value that allows pore cavitation to separate the residual liquid film between the dendrites:

$$\dot{\varepsilon} \geq \frac{1}{R}\left[\frac{\lambda_2^2 \|\nabla T\|}{180\mu_{\text{l}}}\frac{\rho_{\text{L}}}{\rho_{\text{s}}}(p_{\text{m}} - p_{\text{C}}) - v_{\text{T}}\frac{\rho_{\text{s}} - \rho_{\text{L}}}{\rho_{\text{s}}}H\right] \quad \text{(Eq 30)}$$

in which μ_l is the dynamic viscosity of the liquid phase, λ_2 is the secondary dendrite arm spacing, p_{m} is the local pressure in the liquid ahead of the mushy zone, p_{C} is the cavitation pressure, and v_{T} is the velocity of the solidification front. The quantities R and H depend on the solidification path of the alloy:

$$R = \int_{T_2}^{T_1} \frac{g_s^2 F(T)}{g_l^3} dT$$

$$H = \int_{T_2}^{T_1} \frac{g_s^2}{g_l^2} dT$$

$$F(T) = \frac{1}{\|\nabla T\|}\int_{T_2}^{T} g_s dT \quad \text{(Eq 31)}$$

where the integration limits are calibration parameters that also have physical meaning (Ref 83). The upper limit T_1 may be the liquidus or the coherency temperature, while the lower limit T_2 typically is within the solid fraction range of 0.95 to 0.99 (Ref 84).

Case Study: Billet Casting Speed Optimization. A Lagrangian model of temperature, distortion, strain, stress, hot tearing has been applied to predict the maximum speed for continuous casting of steel billets without forming off-corner internal cracks. The two-dimensional transient finite-element thermomechanical model, CON2D (Ref 20, 21), has been used to track a transverse slice through the solidifying steel strand as it moves downward at the casting speed to reveal the entire three-dimensional stress state. The two-dimensional assumption produces reasonable temperature predictions because axial (z-direction) conduction is negligible relative to axial advection (Ref 50). In-plane mechanical predictions are also reasonable because bulging effects are small and the undiscretized casting direction is modeled with the appropriate condition of

generalized plain strain. Other applications with this model include the prediction of ideal taper of the mold walls (Ref 85) and quantifying the effect of steel grade on oscillation mark severity during level fluctuations (Ref 86).

The model domain is an L-shaped region of a two-dimensional transverse section, shown in Fig. 11. Removing the central liquid region saves computation and lessens stability problems related to element "locking." Physically, this "trick" is important in two-dimensional domains because it allows the liquid volume to change without generating stress, which mimics the effect of fluid flow into and out of the domain that occurs in the actual open-topped casting process. Simulations start at the meniscus, 100 mm (4 in.) below the mold top, and extend through the 800 mm (32 in.) long mold and below, for a caster with no submold support. The instantaneous heat flux, given in Eq 32, was based on plant measurements (Ref 45). It was assumed to be uniform around the perimeter of the billet surface in order to simulate ideal taper and perfect contact between the shell and mold. Below the mold, the billet surface temperature was kept constant at its circumferential profile at mold exit. This eliminates the effect of spray cooling practice imperfections on submold reheating or cooling and the associated complication for the stress/strain development. A typical plain carbon steel was studied (0.27% °C, 1.52% Mn, 0.34% Si) with 1500.7 °C (2733 °F) liquidus temperature, and 1411.8 °C (2573 °F) solidus temperature. Constitutive equation and properties are given in the sections "Solid-State Constitutive Models" and "Example of Solid-State Constitutive Equations."

$$q(\mathrm{MW/m^2}) = \begin{cases} 5 - 0.2444t(\mathrm{s}) & t \le 1.0\ \mathrm{s} \\ 4.7556t(\mathrm{s})^{-0.504} & t > 1.0\ \mathrm{s} \end{cases} \quad \text{(Eq 32)}$$

Sample results are presented here for one-quarter of a 120 mm^2 (0.2 $in.^2$) billet cast at speeds of 2.0 and 5.0 m/min (6.5 to 16.5 ft/s). The latter is the critical speed at which hot-tear crack failure of the shell is just predicted to occur. The temperature and axial (z) stress distributions in a typical section through the wide face of the steel shell cast at 2.0 m/min (6.5 ft/s) are shown in Fig. 12 and 13 at four different times during cooling in the mold. Unlike the analytical solution in Fig. 3, the surface temperature drops as time progresses. The corresponding stress distributions are qualitatively similar to the analytical solution (Fig. 4). The stresses increase with time, however, as solidification progresses. The realistic constitutive equations produce a large region of tension near the solidification front. The magnitude of these stresses (as well as the corresponding strains) is not predicted to be enough to cause hot tearing in the mold, however. The results from two different codes reasonably match, demonstrating that the formulations are accurately implemented, convergence has been achieved, and the mesh and time-step refinement are sufficient.

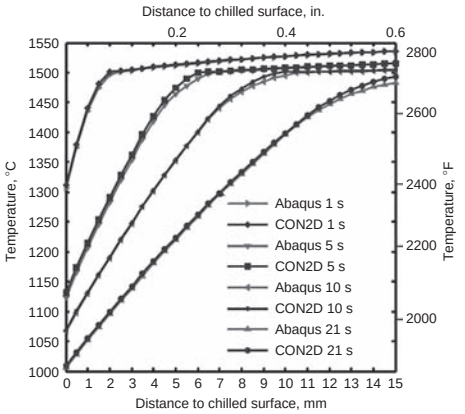

Fig. 12 Temperature distribution along the solidifying slice in continuous casting mold

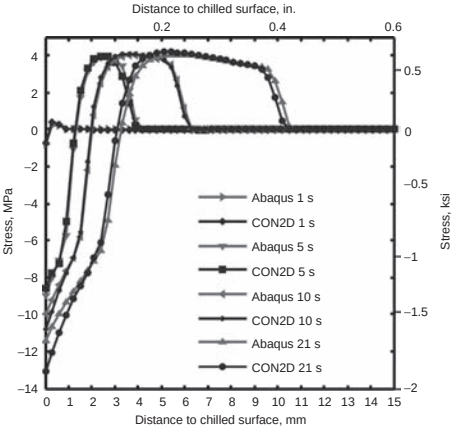

Fig. 13 Lateral (y and z) stress distribution along the solidifying slice in continuous casting mold

Figure 14(a) shows the distorted temperature contours near the strand corner at 200 mm (8 in.) below the mold exit, for a casting speed of 5.0 m/min (16.5 ft/min). The corner region is coldest, owing to two-dimensional cooling. The shell becomes hotter and thinner with increasing casting speed, owing to less time in the mold. This weakens the shell, allowing it to bulge more under the ferrostatic pressure below the mold.

Figure 14(b) shows contours of "hoop" stress constructed by taking the stress component acting perpendicular to the dendrite growth direction, which simplifies to σ_x in the lower right portion of the domain and σ_y in the upper left portion. High values appear at the off-corner subsurface region, due to a hinging effect that the ferrostatic pressure over the entire face exerts around the corner. This bends the shell around the corner and generates high subsurface tensile stress at the weak solidification front in the off-corner subsurface location. This tensile stress peak increases slightly and moves toward the surface at higher casting speed. Stress concentration is less, and the surface hoop stress is compressive at the lower casting speed. This indicates no possibility of surface cracking. However, tensile surface hoop stress is generated below the mold at high speed in Fig. 14(b) at the face center due to excessive bulging. This tensile stress, and the accompanying hot-tear strain, might contribute to longitudinal cracks that penetrate the surface.

Hot tearing was predicted using the criterion in Eq 28 with the critical strain given in Eq 29. Inelastic strain was accumulated for the component oriented normal to the dendrite growth direction, because that is the weakest direction and corresponds to the measurements used to obtain Eq 29. Figure 14(c) shows contours of hot-tear strain in the hoop direction. The highest values appear at the off-corner subsurface region in the hoop direction. Moreover, significantly higher values are found at higher casting speeds. For this particular example, hot-tear strain exceeds the threshold at 12 nodes, all located near the off-corner subsurface region. This is caused by the hinging mechanism around the corner. No nodes fail at the center surface, in spite of the high tensile stress there. The predicted hot-tearing region matches the location of off-corner longitudinal cracks observed in sections through real solidifying shells, such as the one pictured in Fig. 15. The bulged shape is also similar.

Results from many computations were used to find the critical speed to avoid hot-tear cracks as a function of section size and working mold length, presented in Fig. 16 (Ref 46). These predictions slightly exceed plant practice, which is generally chosen by empirical trial and error (Ref 87). This suggests that plant conditions such as mold taper are less than ideal, that other factors limit casting speed, or those speeds in practice could be increased. The qualitative trends are the same.

This quantitative model of hot tearing provides many useful insights into the continuous casting process. Larger section sizes are more susceptible to bending around the corner and so have a lower critical casting speed, resulting in less productivity increase than expected. The trend toward longer molds over the past three decades enables a higher casting speed without cracks by producing a thicker, stronger shell at mold exit.

Conclusions

Mechanical analysis of casting processes is growing in sophistication, accuracy, and phenomena incorporated. Quantitative predictions of temperature, deformation, strain, stress, and hot tearing in real casting processes are becoming possible. Computations are still hampered by the computational speed and limits of mesh resolution, especially for realistic three-dimensional geometries and defect analysis.

ACKNOWLEDGMENT

The authors wish to thank the Continuous Casting Consortium and the National Center

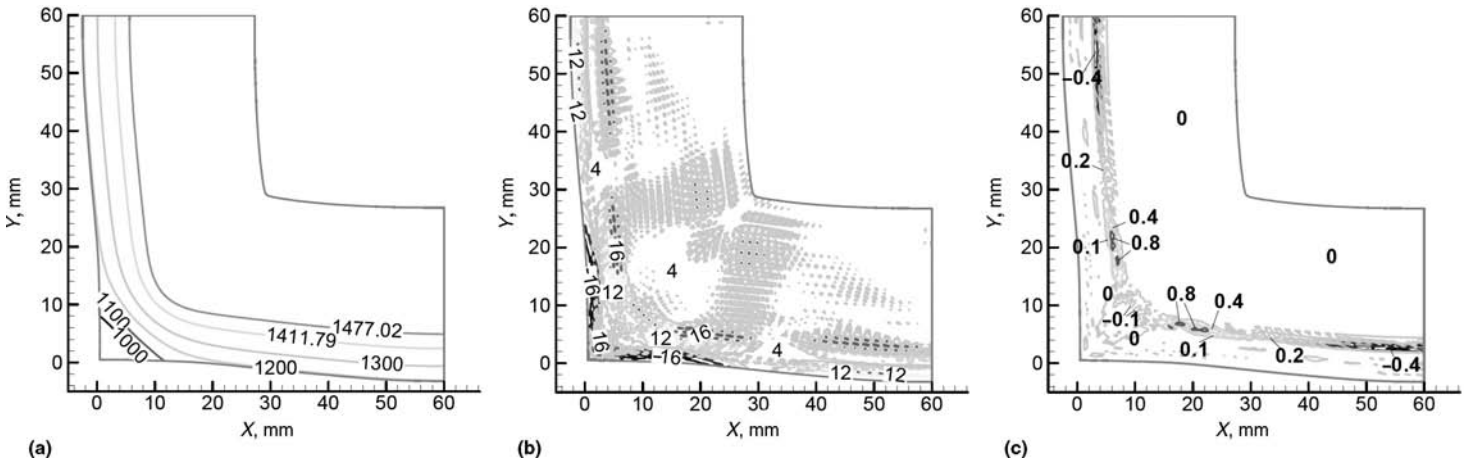

Fig. 14 Distorted contours at 200 mm (8 in.) below mold exit. (a) Temperature. (b) Hoop stress. (c) Hot-tear strain

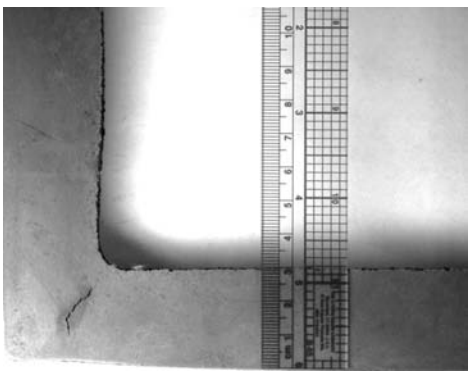

Fig. 15 Off-corner internal crack in breakout shell from a 175 mm (7 in.) square bloom

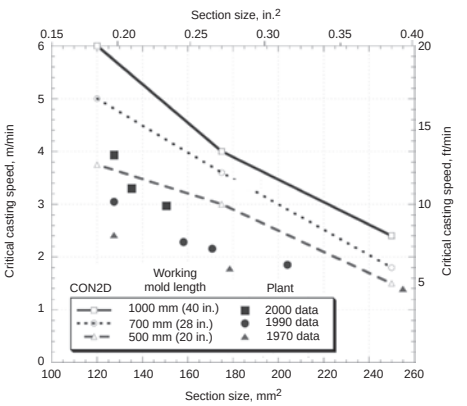

Fig. 16 Comparison of critical casting speeds, based on hot-tearing criterion (Ref 46), and typical plant practice (Ref 87)

for Supercomputing Applications at the University of Illinois, the French Ministry of Industry, the French Technical Center of Casting Industries (CTIF), and the companies ArcelorMittal, Ascometal, Aubert et Duval, Industeel, and PSA Peugeot-Citroën, for support of this work.

REFERENCES

1. G.E. Mase and G.T. Mase, *Continuum Mechanics for Engineers*, 2nd ed., CRC Press, 1999
2. B.G. Thomas, Q. Yuan, S. Sivaramakrishnan, T. Shi, S.P. Vanka, and M.B. Assar, Comparison of Four Methods to Evaluate Fluid Velocities in a Continuous Casting Mold, *ISIJ Int.*, Vol 41 (No. 10), 2001, p 1266–1276
3. Q. Yuan, B. Zhao, S.P. Vanka, and B.G. Thomas, Study of Computational Issues in Simulation of Transient Flow in Continuous Casting, *Steel Res. Int.*, Vol 76 (No. 1, Special Issue: Simulation of Fluid Flow in Metallurgy), 2005, p 33–43
4. Q. Yuan, S. Sivaramakrishnan, S.P. Vanka, and B.G. Thomas, Computational and Experimental Study of Turbulent Flow in a 0.4-Scale Water Model of a Continuous Steel Caster, *Metall. Mater. Trans.*, Vol 35B (No. 5), 2004, p 967–982
5. C. Beckermann, Macrosegregation, in *Encyclopedia of Materials: Science and Technology*, Elsevier, 2001, p 4733–4739
6. G. Lesoult, C.-A. Gandin, and N.T. Niane, Segregation During Solidification with Spongy Deformation of the Mushy Zone, *Acta Mater.*, Vol 51, 2003, p 5263–5283
7. L.C. Nicolli, A. Mo, and M. M'Hamdi, Modeling of Macrosegregation Caused by Volumetric Deformation in a Coherent Mushy Zone, *Metall. Mater. Trans. A*, Vol 36, 2005, p 433–442
8. V.D. Fachinotti, S. Le Corre, N. Triolet, M. Bobadilla, and M. Bellet, Two-Phase Thermo-mechanical and Macrosegregation Modelling of Binary Alloys Solidification with Emphasis on the Secondary Cooling Stage of Steel Slab Continuous Casting, *Int. J. Num. Meth. Eng.*, Vol 67 (No. 10), 2006, p 1341–1384
9. O. Ludwig, C.-L. Martin, J.-M. Drezet, and M. Suéry, Rheological Behaviour of Al-Cu Alloys During Solidification: Constitutive Modelling, Experimental Identification and Numerical Study, *Met. Mater. Trans.*, Vol 36A, 2005, p 1525–1535
10. Y. Estrin, A Versatile Unified Constitutive Model Based on Dislocation Density Evolution, in *Constitutive Modelling—Theory and Application*, Vol MD-vol26/AMD-vol121, ASME, 1991, p 65–75
11. C. Agelet de Saracibar, M. Cervera, and M. Chiumenti, On the Constitutive Modeling of Coupled Thermomechanical Phase-Change Problems, *Int. J. Plast.*, Vol 17, 2001, p 1565–1622
12. J. Sengupta, S.L. Cockcroft, D.M. Maijer, and A. Larouche, Quantification of Temperature, Stress, and Strain Fields During the Start-up Phase of Direct Chill Casting Process by Using a 3D Fully Coupled Thermal and Stress Model for AA5182 Ingots, *Mater. Sci. Eng. A*, Vol 397, 2005, p 157–177
13. J.E. Kelly, K.P. Michalek, T.G. O'Connor, B.G. Thomas, and J.A. Dantzig, Initial Development of Thermal and Stress Fields in Continuously Cast Steel Billets, *Metall. Trans. A*, Vol 19A (No. 10), 1988, p 2589–2602
14. A.E. Huespe, A. Cardona, and V. Fachinotti, Thermomechanical Model of a Continuous Casting Process, *Comput. Meth. Appl. Mech. Eng.*, Vol 182 (No. 3), 2000, p 439–455
15. *MARC Users Manual*, MARC Analysis Research Corp., Palo Alto, CA, 1991
16. "ABAQUS Theory Manual v6.0," Abaqus, Inc., Pawtucket, RI, 2004
17. A. Hakonsen and D. Mortensen, *Modeling of Casting, Welding and Advanced Solidification Processes VII*, TMS, Warrendale, PA, 1995, p 963–970
18. H.G. Fjaer and A. Mo, ALSPEN—A Mathematical Model for Thermal Stresses in DC-Cast Al Billets, *Metall. Trans.*, Vol 21B (No. 6), 1990, p 1049–1061

19. G. Laschet, J. Jakumeit, and S. Benke, Thermo-mechanical Analysis of Cast/Mould Interaction in Casting Processes, *Z. Metallkd*., Vol 95, 2004, p 1087–1096
20. C. Li and B.G. Thomas, Thermo-Mechanical Finite-Element Model of Shell Behavior in Continuous Casting of Steel, *Metall. Mater. Trans. B*, Vol. 35B (No. 6), 2004, p 1151–1172
21. S. Koric and B.G. Thomas, Efficient Thermo-Mechanical Model for Solidification Processes, *Int. J. Num. Meth. Eng*., Vol 66 (No. 12), 2006, p 1955–1989
22. MAGMASOFT, http://www.magmasoft.com, 2007
23. PROCAST, Procast, http://www.esi-group.com/SimulationSoftware/Die_Casting_Solution/Products/ Casting_simulation/, 2007
24. M. Samonds and J.Z. Zhu, Coupled Thermal-Fluid-Stress Analysis of Castings, *Proc. MCWASP IX, Ninth Int. Conf. on Modeling of Casting, Welding and Advanced Solidification Processes*, P.R. Sahm, P.N. Hansen, and J.G. Conley, Ed. (Aachen, Germany), Aug 20–25, 2000, Shaker Verlag, Aachen, 2000, p 80–87
25. J.M. Drezet, A. Bughardt, H.G. Fjaer, and B. Magnin, Thermomechanical Effects in D.C. Casting of Aluminum Alloy: A Numerical Benchmark Study, *Mater. Sci. Forum*, Vol 329–330, 2000, p 493–500
26. H.G. Fjaer and A. Hakonsen, The Mechanism of Pull-in During DC-Casting of Aluminum Sheet Ingots, *Light Metals 1997*, TMS, Warrendale, PA, 1997, p 683–690
27. A. Mo, M. Rappaz, and L.L. Martin, *Aluminum*, Vol 78 (No. 10), 2002, p 856–864
28. J.M. Drezet, A. Bughardt, H.G. Fjaer, and B. Magnin, *Mater. Sci. Forum*, Vol 329–330, 2000, p 493–500
29. A. Henry, *Light Metal Age*, Vol 58 (No. 7–8), 2000, p 66–67
30. M. Bellet, O. Jaouen, and I. Poitrault, An ALE-FEM Approach to the Thermomechanics of Solidification Processes with Application to the Prediction of Pipe Shrinkage, *Int. J. Num. Meth. Heat Fluid Flow*, Vol 15, 2005, p 120–142
31. O.C. Zienkiewicz and R.L. Taylor, *The Finite Element Method*, 4th ed., McGraw Hill, 1988
32. J.-M. Drezet, B. Commet, H.G. Fjaer, and B. Magnin, Stress-Strain Computations of the DC Casting Process of Aluminum Alloy: A Sensitivity Study on Material Properties, *Proc. MCWASP IX, Ninth Int. Conf. on Modeling of Casting, Welding and Advanced Solidification Processes*, P.R. Sahm, P.N. Hansen, and J.G. Conley, Ed., (Aachen, Germany), Aug 20–25, 2000, Shaker Verlag, Aachen, 2000, p 33–40
33. M. Bellet and V.D. Fachinotti, ALE Method for Solidification Modelling, *Comput. Meth. Appl. Mech. Eng*., Vol 193, 2004, p 4355–4381
34. Thercast, presentation, www.transvalor.com and www.scconsultants.com, 2007
35. M. Chiumenti, M. Cervera, and C.A.d. Saracibar, Coupled Thermomechanical Simulation of Solidification and Cooling Phases in Casting Processes, *Proc. MCWASP XI, 11th Int. Conf. on Modeling of Casting, Welding and Advanced Solidification Processes*, C.-A. Gandin and M. Bellet, Ed., TMS, Warrendale, PA, 2006, p 201–208
36. P. Kozlowski, B.G. Thomas, J. Azzi, and H. Wang, Simple Constitutive Equations for Steel at High Temperature, *Metall. Trans. A*, Vol 23A (No. 3), 1992, p 903–918
37. P.J. Wray, Plastic Deformation of Delta-Ferritic Iron at Intermediate Strain Rates, *Metall. Trans. A*, Vol 7A, Nov 1976, p 1621–1627
38. P.J. Wray, Effect of Carbon Content on the Plastic Flow of Plain Carbon Steels at Elevated Temperatures, *Metall. Trans. A*, Vol 13A (No. 1), 1982, p 125–134
39. T. Suzuki, K.H. Tacke, K. Wunnenberg, and K. Schwerdtfeger, Creep Properties of Steel at Continuous Casting Temperatures, *Ironmaking Steelmaking*, Vol 15 (No. 2), 1988, p 90–100
40. F. Costes, A. Heinrich, and M. Bellet, 3D Thermomechanical Simulation of the Secondary Cooling Zone of Steel Continuous Casting, *Proc. MCWASP X, Tenth Int. Conf. on Modeling of Casting, Welding and Advanced Solidification Processes*, D.M. Stefanescu, J.A. Warren, M.R. Jolly, and M.J.M. Krane, Ed., TMS, Warrendale, PA, 2003, p 393–400
41. D.L. Donsbach and M.W. Moyer, Ultrasonic Measurement of Elastic Constants at Temperatures from 20 to 1100 °C, *Ultrasonic Materials Characterization*, Special Pub. 596, H. Berger and M. Linzer, Ed., National Bureau of Standards, 1980
42. O.M. Puhringer, Strand Mechanics for Continuous Slab Casting Plants, *Stahl Eisen*, Vol 96 (No. 6), 1976, p 279–284
43. D.R. Hub, Measurement of Velocity and Attenuation of Sound in Iron up to the Melting Point, *Proc. IVth Int. Vong. Acoustics* (Copenhagen), 1962, paper 551
44. H. Mizukami, K. Murakami, and Y. Miyashita, Mechanical Properties of Continuously Cast Steels at High Temperatures, *Tetsu-to-Hagane*, Vol 63 (No. 146), 1977, p S652
45. C. Li, and B.G. Thomas, Maximum Casting Speed for Continuous Cast Steel Billets Based on Sub-Mold Bulging Computation, *Steelmaking Conf. Proc*., Vol 85 (Nashville, TN), March 10–13, 2002, ISS, Warrendale, PA, 2002, p 109–130
46. C. Li and B.G. Thomas, Thermo-Mechanical Finite Element Model of Bulging and Hot Tearing During Continuous Casting of Steel Billets, *Modeling of Casting, Welding, and Advanced Solidification Processes*, Vol X, D. Stefanescu, J. Warren, M. Jolly, and M. Krane, Ed. (San Destin, FL), May 25–30, 2003, TMS, Warrendale, PA, 2003, p 385–392
47. K. Harste, A. Jablonka, and K. Schwerdtfeger, Shrinkage and Formation of Mechanical Stresses During Solidification of Round Steel Strands, *Fourth Int. Conf. on Continuous Casting* (Centres de Recherches Metallurgiques and Verein Deutscher Eisenhuttenleute), Stahl und Eisen, Brussels, 1988, p 633–644
48. K. Harste, "Investigation of the Shrinkage and the Origin of Mechanical Tension During the Solidification and Successive Cooling of Cylindrical Bars of Fe-C Alloys," Ph.D. dissertation thesis, Technical University of Clausthal, 1989
49. I. Jimbo and A. Cramb, The Density of Liquid Iron-Carbon Alloys, *Metall. Trans. B*, Vol 24B, 1993, p 5–10
50. Y. Meng and B.G. Thomas, Heat Transfer and Solidification Model of Continuous Slab Casting: CON1D, *Met. Mater. Trans*., Vol 34B (No. 5), 2003, p 685–705
51. C.V. Madhusudana and L.S. Fletcher, Contact Heat Transfer—The Last Decade, *AIAA J*., Vol 24, 1985, p 510–523
52. M. Rappaz, M. Bellet, and M. Deville, Numerical Modeling in Materials Science and Engineering, in *Springer Series in Computational Mathematics*, Springer Verlag, Berlin, 2003
53. S. Nemat-Nasser, and Y.F. Li, An Explicit Algorithm for Large-Strain, Large-Strain Rate Elastic-Viscoplasticity, *Comput. Meth. Appl. Mech. Eng*., Vol 48, 1992, p 205–219
54. A.M. Lush, G. Weber, and L. Anand, An Implicit Time-integration Procedure for A Set of Internal Variable Constitutive Equations for Isotropic Elastic-Viscoplasticity, *Int. J. Plast*., Vol 5, 1989, p 521–549
55. H. Zhu, "Coupled Thermal-Mechanical Finite-Element Model with Application to Initial Solidification," Thesis, University of Illinois, 1993
56. R. Glowinski and P.L. Tallee, Augmented Lagrangian and Operator-Splitting Methods in Non-linear Mechanics, Studies in Applied Mathematics, *SIAM*, Vol 9, 1989, p 295
57. P. Wriggers and G. Zavarise, On Contact between Three-Dimensional Beams Undergoing Large Deflections, *Commun. Num. Meth. Eng*., Vol 13, 1997, p 429–438
58. O. Jaouen and M. Bellet, A Numerical Mechanical Coupling Algorithm for Deformable Bodies: Application to Part/Mold Interaction in Casting Process, *Proc. Eighth Int. Conf. on Modelling of Casting, Welding and Advanced Solidification Processes*, B.G. Thomas and C. Beckermann, Ed. (San Diego, CA), June 7–12, 1998, TMS, Warrendale, PA, 1998, p 739–746
59. J.H. Weiner and B.A. Boley, Elasto-plastic Thermal Stresses in a Solidifying Body, *J. Mech. Phys. Solids*, Vol 11, 1963, p 145–154
60. M. Bellet, C. Aliaga, and O. Jaouen, Finite Elements for a Thermomechanical

Analysis of Solidification Processes, *Modeling of Casting, Welding, and Advanced Solidification Processes IX*, Shaker Verlag GmbH, Aachen, 2000, p 10–17
61. S. David and P. Auburtin, Numerical Simulation of Casting Processes. Benefits of Thermomechanical Simulation in Automotive Industry, *Conference Matériaux 2002, Tours, France, Proc*., Vol on CD, Université Technologique de Belfort-Montbéliard, 2002, p 5 (in French)
62. K. Miyazawa and K. Schwerdtfeger, Macrosegregation in Continuously Cast Steel Slabs: Preliminary Theoretical Investigation on the Effect of Steady State Bulging, *Arch. Eisenhütten*., Vol 52 (No. 11), 1981, p 415–422
63. G. Lesoult and S. Sella, Analysis and Prevention of Centreline Segregation During Continuous Casting of Steel Related to Deformation of the Solid Phase, *Solid State Phenom*., Vol 3, 1988, p 167–178
64. M. Bellet and A. Heinrich, A Two-Dimensional Finite Element Thermomechanical Approach to a Global Stress-Strain Analysis of Steel Continuous Casting, *ISIJ Int*., Vol 44, 2004, p 1686–1695
65. K. Wünnenberg and D. Huchingen, Strand Bulging between Supporting Rollers During Continuous Slab Casting, *Stahl Eisen*, Vol 98 (No. 6), 1978, p 254–259
66. T. Kajitani, J.-M. Drezet, and M. Rappaz, Numerical Simulation of Deformation-Induced Segregation in Continuous Casting of Steel, *Metall. Mater. Trans. A*, Vol 32, 2001, p 1479–1491
67. N. Triolet and M. Bobadilla, Mastering Steel Slab Internal Soundness and Surface Quality Issues through Thermomechanical Modelling of Continuous Casting, *Proc. MCWASP-XI, 11th Int. Conf. on Modelling of Casting, Welding, and Advanced Solidification Processes*, C.A. Gandin and M. Bellet, Ed. (Opio, France), May 28 to June 2, 2006), TMS, Warrendale, PA, 2006, p 753–760
68. D.G. Eskin, Suyitno, and L. Katgerman, Mechanical Properties in the Semi-Solid State and Hot Tearing of Aluminum Alloys, *Prog. Mater. Sci*., Vol 49, 2004, p 629–711
69. T.W. Clyne and G.J. Davies, Comparison between Experimental Data and Theoretical Predictions Relating to Dependence of Solidification Cracking on Composition, *Solidification and Casting of Metals*, The Metals Society, London, 1979, p 275–278
70. K. Kinoshita, T. Emi, and M. Kasai, Thermal Elasto-plastic Stress Analysis of Solidifying Shell in Continuous Casting Mold, *Tetsu-to-Hagane*, Vol 65 (No. 14), 1979, p 2022–2031
71. J.O. Kristiansson, Thermal Stresses in the Early Stage of Solidification of Steel, *J. Thermal Stresses*, Vol 5, 1982, p 315–330
72. B.G. Thomas, I.V. Samarasekera, and J.K. Brimacombe, Mathematical Model of the Thermal Processing of Steel Ingots, Part II: Stress Model, *Metall. Trans. B*, Vol 18B (No. 1), 1987, p 131–147
73. K. Okamura and H. Kawashima, Calculation of Bulging Strain and its Application to Prediction of Internal Cracks in Continuously Cast Slabs, *Proc. Int. Conf. Comp. Ass. Mat. Design Proc. Simul*., ISIJ, Tokyo, 1993, p 129–134
74. P. Ackermann, W. Kurz, and W. Heinemann, In Situ Tensile Testing of Solidifying Aluminum and Al-Mg Shells, *Mater. Sci. Eng*. Vol 75, 1985, p 79–86
75. C. Bernhard, H. Hiebert, and M.M. Wolf, Simulation of Shell Strength Properties by the SSCT Test, *ISIJ Int. (Japan)*, Vol 36 (Suppl. Science and Technology of Steelmaking), 1996, p S163–S166
76. M. Suzuki, C. Yu, and T. Emi, In-Situ Measurement of Tensile Strength of Solidifying Steel Shells to Predict Upper Limit of Casting Speed in Continuous Caster with Oscillating Mold, *ISIJ Int., Iron Steel Inst. Jpn*., Vol 37 (No. 4), 1997, p 375–382
77. A. Yamanaka, K. Nakajima, K. Yasumoto, H. Kawashima, and K. Nakai, Measurement of Critical Strain for Solidification Cracking, *Modelling of Casting, Welding, and Advanced Solidification Processes*, Vol V, M. Rappaz, M.R. Ozgu, and K.W. Mahin, Ed., (Davos, Switzerland), TMS, Warrendale, PA, 1990, p 279–284
78. A. Yamanaka, K. Nakajima, and K. Okamura, Critical Strain for Internal Crack Formation in Continuous Casting, *Ironmaking Steelmaking*, Vol 22 (No. 6), 1995, p 508–512
79. P. Wisniewski and H.D. Brody, Tensile Behavior of Solidifying Aluminum Alloys, *Modelling of Casting, Welding, and Advanced Solidification Processes*, Vol V, M. Rappaz, M.R. Ozgu, and K.W. Mahin, Ed., (Davos, Switzerland), TMS, Warrendale, PA, 1990, p 273–278
80. Y.-M. Won, T.J. Yeo, D.J. Seol, and K.H. Oh, A New Criterion for Internal Crack Formation in Continuously Cast Steels, *Metall. Mater. Trans. B*, Vol 31B, 2000, p 779–794
81. U. Feurer, Mathematisches modell der Warmrissneigung von binären aluminium legierungen, *Giessereiforschung*, Vol 28, 1976, p 75–80
82. M. Rappaz, J.-M. Drezet, and M. Gremaud, A New Hot-Tearing Criterion, *Metall. Mater. Trans. A*, Vol 30A (No. 2), 1999, p 449–455
83. J.M. Drezet and M. Rappaz, Prediction of Hot Tears in DC-Cast Aluminum Billets, *Light Metals*, J.L. Anjier, Ed., TMS, Warrendale, PA, 2001, p 887–893
84. M. M'Hamdi, S. Benum, D. Mortensen, H. G. Fjaer, and J.M. Drezet, The Importance of Viscoplastic Strain Rate in the Formation of Center Cracks During the Start-up Phase of Direct-Chill Cast Aluminium Extrusion Ingots, *Metall. Mater. Trans. A*, Vol 34, 2003, p 1941–1952
85. B.G. Thomas and C. Ojeda, Ideal Taper Prediction for Slab Casting, *ISSTech Steelmaking Conference* (Indianapolis, IN), April 27–30, 2003, Vol 86, 2003, p 396–308
86. J. Sengupta and B.G. Thomas, Effect of a Sudden Level Fluctuation on Hook Formation During Continuous Casting of Ultra-Low Carbon Steel Slabs, *Modeling of Casting, Welding, and Advanced Solidification Processes XI (MCWASP XI) Conference*, C.Z. Gandin, M. Bellet, and J.E. Allison, Ed. (Opio, France, May 28 to June 2, 2006), TMS, Warrendale, PA, 2006, p 727–736
87. E. Howard and D. Lorento, Development of High Speed Casting, *1996 Electric Furnace Conference Proceedings*, (Dallas, TX), Dec 9–12, 1996, ISS, Warrendale, PA, 1996